Pergamon

Mg isotope heterogeneity in the Allende meteorite measured by UV laser ablation–MC–ICPMS and comparisons with O isotopes

EDWARD D. YOUNG,* RICHARD D. ASH, ALBERT GALY, and NICK S. BELSHAW

Department of Earth Sciences, University of Oxford, Parks Road, Oxford OX1 3PR, United Kingdom

Abstract—First results from a new UV laser ablation MC–ICPMS method for measuring Mg isotope ratios *in situ* in meteoritical materials show that there are mass-dependent variations in $\delta^{25}Mg$ and $\delta^{26}Mg$ up to 1.5 ‰ per amu in chondrules and 0.3‰ per amu in a CAI from the Allende meteorite. In both cases the mass-dependent fractionation is associated with alteration. Comparisons with laser ablation O isotope data indicate that incorporation of pre-existing grains of forsterite with distinct Mg and O isotopic compositions and post-formation alteration both contributed to the variability in Mg isotope ratios in the chondrules, resulting in a correlation between high $\delta^{25}Mg$ and low $\Delta^{17}O$. The laser ablation analyses of the CAI show that high-precision determinations of both $\delta^{25}Mg$ and $\delta^{26}Mg$ can be used to discriminate features of the $^{26}Al–^{26}Mg$ isotope system that are relevant to chronology from those that result from element mobility. *Copyright © 2002 Elsevier Science Ltd*

1. INTRODUCTION

Magnesium is a major element in minerals that occur in a wide range of geological environments. The large relative differences in masses between the three stable isotopes ^{24}Mg, ^{25}Mg, and ^{26}Mg have motivated searches for differences in $^{25}Mg/^{24}Mg$ and $^{26}Mg/^{24}Mg$ among geological materials (e.g., Daughtry et al., 1962). Initial reports of large fractionations on the order of tens per mil were not verified by later work (Shima, 1964) and, until recently, precise measurements of mass-dependent fractionation of Mg isotopes in rocks was not possible. Investigators have instead focussed on detection of nonmass dependent, or "anomalous," Mg isotope effects. From these studies came discovery of radiogenic ^{26}Mg in primitive meteorites (Gray and Compston, 1974; Lee and Papanastassiou, 1974).

Mass-dependent fractionation among the Mg isotopes in meteorites and other rocks has been difficult to measure because the analytical precision of the two methods used, thermal ionization mass spectrometry (TIMS) and secondary ion mass spectrometry (SIMS), is limited by instrumental fractionation. However, with the advent of multiple collection inductively coupled plasma-source mass spectrometry (MC–ICPMS), measurements of both $^{25}Mg/^{24}Mg$ and $^{26}Mg/^{24}Mg$ in minerals can now be made with a precision of approximately $+/−0.10$ per mil per amu (2σ) or better (Galy et al., 2000), representing a tenfold improvement over other techniques. To date the MC–ICPMS technology has been applied to Mg in dilute acid solutions extracted from minerals by acid digestion and chemical purification.

In this paper we describe a UV laser-based Multiple Collection Inductively Coupled Plasma-source Mass Spectrometry

(MC–ICPMS) method for measuring $^{25}Mg/^{24}Mg$ and $^{26}Mg/^{24}Mg$ *in situ* in minerals with a precision of $+/−0.15$ per mil (2σ) and $+/−0.25$ per mil (2σ), respectively. The method is used to show that there are mass-dependent variations in Mg isotope ratios within chondrules from the Allende meteorite on the order of 1.5 per mil per amu, representing a level of mass-dependent isotope heterogeneity that is comparable to oxygen in these objects. There are no resolvable departures from mass-dependent fractionation evident in the chondrule Mg isotopes, but correlations between $^{25}Mg/^{24}Mg$ (and $^{26}Mg/^{24}Mg$) and nonmass dependent variations in O isotope ratios suggest that both inheritance and alteration could have contributed to Mg isotope heterogeneity in chondrules. We also present analyses of a CAI from Allende demonstrating unequivocally that ^{26}Al was present in the low-Al minerals in the inclusion, and that open-system migration of Mg was the likely cause of an *apparent* difference in initial $^{26}Al/^{27}Al$ between altered and unaltered parts of the CAI.

2. METHOD

2.1. Laser Ablation

A Lambda Physik Complex 110™ ArF (193 nm) excimer laser is used to vaporize the target materials. An aperture illuminated by 193 nm laser light is imaged onto the sample surface with a 38 mm focal length lens (25 × magnification). The beam delivery system was built by New Wave Research (DUV™). Pulse energies exiting the laser for these experiments ranged from 116 to 129 mJ. Pulses were delivered to the sample with approximately 1% efficiency at a repetition rate of 1 Hz. Most experiments were run with the sample at the image plane of the laser beam, producing shallow cylindrical pits with steep walls and flat bottoms amenable to inspection by electron beam methods (e.g., backscattered electron imaging, EDS analysis). For the data reported here the pit diameters are all 100 μm and fluence at the ablation spots was between 4 and 5 J cm^{-2}. Our best estimate for the depth of the pits is 30 μm.

* Author to whom correspondence should be addressed (eyoung@ess.ucla.edu).
Present address: Institute of Geophysics and Planetary Physics and Department of Earth & Space Sciences, University of California Los Angeles, 595 Charles E. Young Dr. East, Geology Building, Los Angeles, CA 90095, USA.
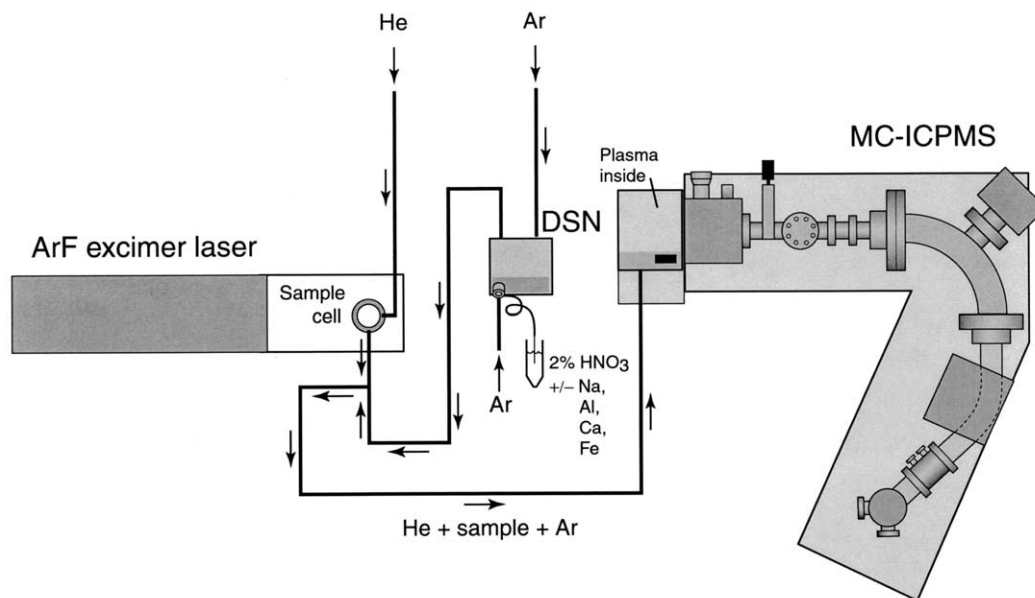
Fig. 1. Schematic illustration of the experimental apparatus used to measure Mg isotope ratios in minerals by UV laser ablation and MC–ICPMS. Tubing connecting the desolvating nebulizer (DSN), sample chamber, and mass spectrometer is Tygon™ or Teflon™ lined Tygon™. The connection between sample chamber and DSN permits evaluation of matrix effects in the plasma source.

2.2. Sample Delivery

The sample cell is flushed with helium gas during laser ablation. Helium is directed toward the plume of plasma above the sample surface. A low pressure of He is used (< 0.1 bar above atmospheric) in order to allow the plasma plume formed during ablation to expand away from the sample surface. Free expansion minimizes fractionation attending sample deposition around the ablation pits. Helium carrying the ablation products from the chamber is combined with dry Ar exiting a desolvating nebulizer (CETAC Aridus™). The mixture of He and Ar delivers the sample to the plasma torch of the MC–ICPMS instrument. With this configuration it is possible to dope the plasma ion source with elements extrinsic to the ablation samples by aspirating dilute acid solutions during ablation (Fig. 1). We used this capability to test the effects of various elements on the laser ablation results (see Sec. 3).

2.3. Mass Spectrometry

Isotope ratios are measured using a Nu Instruments multiple-collector double-focussing magnetic-sector mass spectrometer. The instrument has variable dispersion by virtue of a zoom lens and a fixed array of 12 Faraday collectors (amplifier resistance = 10^{11} Ω for each collector). Magnesium peaks with flat tops are obtained with a working mass resolution of about 300. The laser trigger is controlled by the mass spectrometer software to allow synchronization of laser ablation and ion beam detection. Magnesium isotope ratios are measured in 5×10 s integrations following a 10 s incubation period of ablation during which time the ablation from pulse to pulse becomes more uniform.

We use either a three- or four-step analysis scheme facili-

tated by the MC–ICPMS instrument's variable dispersion optics and fast-scanning laminated magnet. Following analysis of Mg isotope ratios, and while still ablating with the laser, the mass spectrometer magnet and zoom lens are switched rapidly for simultaneous measurement of m/z 21, 22, and 23, permitting calculation of $^{48}Ca^{++}/^{24}Mg^{+}$ from the measured $^{42}Ca^{++}$ and $^{44}Ca^{++}$ signals and Na/Mg from the $^{23}Na^{+}$ signal. Next the instrument is configured to measure m/z 25, 26, and 27 in order to obtain $^{27}Al/^{24}Mg$ from each ablation pit. Finally, for a subset of analyses, the configuration is switched to count m/z 54, 56, and 57, affording estimates of $^{56}Fe/^{24}Mg$ from each pit. The latter includes an isobaric interference from $^{40}Ar^{16}O^{+}$ of approximately 10 to 20 mV (typical 24 signals are in the 1 to 5 V range) but this ratio is used only as an indication of Fe/Mg. The interval between steps is 2 s and the Ca, Na, Al, and Fe measurements are made with 2×10 s integrations, resulting in a total analysis time of about 2 minutes. During the analysis a total of ≈ 130 laser pulses will have been delivered to the sample surface, the first 60 of which are used for the isotopic analysis of Mg. Values for inter-element isotope ratios (e.g., $^{27}Al/^{24}Mg$) are obtained without the high precision afforded by simultaneous measurement because we chose to avoid changing the magnet and zoom settings between Mg isotope ratio measurement blocks. However, the precision of the inter-element ratios (approximately 2 to 4 % relative) is within tolerable limits for the intended applications (e.g., calculating initial values for $^{26}Al/^{27}Al$ and monitoring potential isobaric interferences).

2.4. Calibration and Precision

Magnesium isotope ratios of laser ablation samples are calibrated by alternating the measurements of samples with mea-

Table 1. Analyses of olivine and cpx from mantle xenolith JL-1. Laser data based on USNM 136718 olivine $\delta^{25}Mg = 1.7\%_0$.

Sample	$\delta^{25}Mg_{SRM\ 980}$
JL-1 ol acid digestion	**1.19**
JL-1 ol laser run 2152	0.9
JL-1 ol laser run 2154	1.6
JL-1 ol laser run 2156	1.5
JL-1 ol laser run 2158	1.4
JL-1 ol laser run 2160	0.9
JL-1 ol laser run 2273	1.6
JL-1 ol laser run 2274	1.2
Mean JL-1 ol by laser	**1.3 +/− 0.6 2σ**
JL-1 cpx acid digestion	**1.76**
JL-1 cpx laser run 2296	1.8
JL-1 cpx laser run 2334	1.7
JL-1 cpx laser run 2352	1.7
Mean JL-1 cpx by laser	**1.7 +/− 0.1 2σ**

surements of USNM 136718 forsterite. This sample-standard scheme eliminates the need for instrumental mass fractionation corrections. There is also no need to normalize $^{26}Mg/^{24}Mg$ to a prescribed $^{25}Mg/^{24}Mg$ (nor vice versa), allowing independent measurements of the two isotope ratios. Stability of the instrument is more than sufficient to allow three or four successive pits to be analyzed between standards (often ≈10 analyses can be made without significant drift). Where rare drift is detected, sample analyses are discarded. The Mg isotopic ratios for USNM 136718 forsterite were determined by comparisons with a grain of mantle olivine (JL-1 ol) and a grain of mantle clinopyroxene (JL-1 cpx). Magnesium isotope ratios for the mantle minerals were determined by analysis of multiple grains and comparison with the SRM 980 magnesium standard using MC–ICPMS (Table 1). In the latter experiments, Mg was extracted from the mineral separates by acid digestion and purified by chemical and chromatographic methods (Galy, unpublished). Scatter in the laser ablation analyses of JL-1 olivine is evidently caused by sample heterogeneity as the average is identical to the bulk analysis.

All analyses are reported as per mil deviations in sample magnesium (SA) from the SRM 980 magnesium standard where $\delta^{25}Mg = [(^{25}Mg/^{24}Mg)_{SA}/(^{25}Mg/^{24}Mg)_{SRM\ 980} - 1]$ 10^3 and $\delta^{26}Mg = [(^{26}Mg/^{24}Mg)_{SA}/(^{26}Mg/^{24}Mg)_{SRM\ 980} - 1]$ 10^3. The certified isotope ratios for the SRM 980 magnesium standard are $^{25}Mg/^{24}Mg = 0.126\ 63 +/− 0.000\ 13$ and $^{26}Mg/$

$^{24}Mg = 0.139\ 32 +/− 0.000\ 26$ (Catanzaro et al., 1966). We used these values to convert the $\delta^{25}Mg$ and $\delta^{26}Mg$ values to ratios.

Replicate analyses of USNM 136718 indicate an analytical precision of +/− 0.15‰ 2σ for $\delta^{25}Mg$, +/− 0.25‰ 2σ for $\delta^{26}Mg$ (e.g., Tables 2–5), and +/− 0.20% 2σ for $\delta^{26}Mg^* = \delta^{26}Mg - \delta^{25}Mg /0.52$ (0.52 being the slope of the terrestrial mass fractionation line, Galy et al., 2001). Measured $^{27}Al/^{24}Mg$ were verified by comparison with Al/Mg obtained by characteristic x-ray analysis (EDS). Instrumental fractionation of $^{27}Al/^{24}Mg$ varies with the flow rate of He from the ablation chamber to the plasma source. Tests with laser ablation and dilute solutions show that measured $^{27}Al/^{24}Mg$ values are within about 6% of true values when He flow is minimized in our system. Higher flow rates cause measured $^{27}Al^+/^{24}Mg^+$ to decrease. The data in this study were collected with the minimum He flow rate so that no correction was applied to the measured $^{27}Al^+/^{24}Mg^+$. Further tests are required to explore the accuracy of $^{27}Al/^{24}Mg$ measurements by laser ablation in a variety of materials. The precision of the $^{27}Al/^{24}Mg$ determinations reported here is approximately 2%.

3. TESTS FOR INTERELEMENTAL EFFECTS

3.1. Interferences

Laser ablation liberates all of the elements comprising the target material. Isotope ratio analysis by laser ablation is therefore susceptible to spurious shifts in $^{25}Mg/^{24}Mg$ and $^{26}Mg/$ ^{24}Mg from mass spectrum interferences when analyzing multielement materials. Potential interfering species include $^{48}Ti^{++}$, $^{50}Ti^{++}$, $^{48}Ca^{++}$, $^{50}Cr^{++}$, $^{52}Cr^{++}$, CN^+, CC^+ and various hydrides (e.g., C_2H^+). The effects of hydrides are removed, at least when analyzing anhydrous minerals as in this study, by comparing samples with standards under similar operating conditions (Galy et al., 2001). Chromium concentrations were low enough that the effects of doubly ionized Cr could be ignored. Of the 76 analyses presented here, two are of materials with appreciable Ti concentrations (the Ti-bearing fassaites). Comparing these two analyses with the Ti-poor analyses shows that there is no correlation between Ti abundance in the target and apparent excesses in $m/z = 24$ counts (see below), suggesting that there are no Ti interference effects in the two analyses of Ti-bearing minerals (Ti interferes with both 24 and 25 but has the greatest influence on the former).

Table 2. Laser ablation analyses of USNM 136718 forsterite with and without Fe added to the plasma source of the MC–ICPMS instrument. Concentrations refer to Fe in 2% nitric acid solution aspirated through the desolvating nebulizer during ablation. Values in column 2 are as measured.

Run No. and sample	$^{56}Fe^+/^{24}Mg^+$	$\delta^{25}Mg_{SRM\ 980}$	$\delta^{26}Mg_{SRM\ 980}$
2885 USNM 136718	0.39	1.63	3.09
2886 USNM 136718 + 3.2 ppm Fe	1.99	1.83	3.44
2887 USNM 136718	0.39	1.69	3.34
2888 USNM 136718 + 3.2 ppm Fe	2.00	1.66	3.25
2889 USNM 136718	0.39	1.77	3.35
2890 USNM 136718 + 3.2 ppm Fe	2.00	1.62	3.12
2891 USNM 136718	0.38	1.73	3.29
2892 USNM 136718 + 3.2 ppm Fe	1.91	1.70	3.28
Mean with no Fe added	**0.39**	**1.70 +/− 0.12 (2σ)**	**3.27 +/− 0.24 (2σ)**
Mean with Fe added	**1.98**	**1.70 +/− 0.18 (2σ)**	**3.27 +/− 0.26 (2σ)**

Table 3. Laser ablation analyses of USNM 136718 forsterite with and without Al added to the plasma source of the MC–ICPMS instrument. Concentrations refer to Fe in 2% nitric acid solution aspirated through the desolvating nebulizer during ablation. The laser missed the target for run 2955. Values in column 2 are as measured.

Run No. and sample	$^{27}Al^+/^{24}Mg^+$	$\delta^{25}Mg_{SRM\ 980}$	$\delta^{26}Mg_{SRM\ 980}$
2949 USNM 136718	0.00	1.66	3.36
2950 USNM 136718 + 5.0 ppm Al	2.84	1.73	3.47
2951 USNM 136718	0.00	1.71	3.25
2952 USNM 136718 + 5.0 ppm Al	2.58	1.64	3.21
2953 USNM 136718	0.00	1.73	3.29
2954 USNM 136718 + 5.0 ppm Al	2.69	1.83	3.46
2956 USNM 136718 + 5.0 ppm Al	2.62	1.79	3.39
Mean with no Al added	**0.00**	**1.70 +/− 0.07 (2σ)**	**3.30 +/− 0.12 (2σ)**
Mean with Al added	**2.68**	**1.75 +/− 0.17 (2σ)**	**3.38 +/− 0.24 (2σ)**

The effects of CN^+ are present even when analyzing nominally C-free samples when N_2 is used in the nebulizer gas flow. Excluding N_2 from the nebulizer gas eliminates the problem.

The concentration of Ca sufficient to bias measured magnesium isotope ratios was determined empirically by aspirating solutions of 1 to ≈200 ppm Ca in 2% HNO_3 through the desolvating nebulizer and into the sample carrier gas during laser ablation of USNM 136718 forsterite. Because our mass resolution was too low to resolve $^{48}Ca^{++}$ and $^{24}Mg^+$ we used $^{44}Ca^{++}$ as a proxy for $^{48}Ca^{++}$ in order to calculate the amount of $^{48}Ca^{++}$ entering the source. Measurable interference on $m/z = 24$ signals due to the presence of $^{48}Ca^{++}$ occurs when the concentrations of Ca reaching the plasma source are sufficient to produce $^{44}Ca^{++}/^{24}Mg^+$ voltage ratios > 1 per mil (Fig. 2, Table 5). The effect of $^{48}Ca^{++}$ interference is migration of measured Mg isotope ratios along a line with a slope of 1 on the Mg three-isotope plot. Comparing the laser ablation Mg isotope ratio measurements of forsterite in the presence of Ca with the calculated effect of $^{48}Ca^{++}$ shows that concentrations of Ca large enough to cause significant isobaric interference effects also cause mass-dependent fractionation of the Mg isotopes (Fig. 2). On the basis of these experiments that demonstrate the ill effects of Ca, the Ca doubly ionized species are monitored routinely during laser ablation analyses. None of the materials analyzed as part of this study had sufficient Ca to produce interference effects greater than 0.09 per mil (i.e., $^{44}Ca^{++}/^{24}Mg^+$ ratios were all ≤1 per mil and $^{48}Ca^{++}/^{44}Ca^{++}$ is very close to 0.09) or measurable mass-dependent fractionation effects. This includes melilites from the calcium–alumi-num-rich inclusion (CAI) 3576-1 from the Allende meteorite in which Ca/Mg is as high as 6.

3.2. Matrix Effects

So-called "matrix effects" can also cause unwanted shifts in isotope ratios when measurements are made in the presence of other elements in the plasma source. Matrix effects are effective changes in instrument fractionation related to chemistry in the plasma. The mass fractionation caused by Ca (Fig. 2) is an example of such an effect. Variability in the concentrations of Fe, Al, and Na (Na is known to be problematical in other ICPMS applications) in the materials of interest in this study necessitated evaluation of the potential effects of these elements (in addition to the Ca tests described above). The potential for matrix effects was investigated by entraining 2% HNO_3 solutions with ranges in concentrations of Fe, Al, and Na into the sample carrier gas during laser ablation of USNM 136718 forsterite. Typical results are shown in Tables 2–4.

We find that relevant concentrations of Fe, Al, and Na do not influence measured Mg isotope ratios at the 0.1‰ per amu level of detection during laser ablation. For example, adding Fe to the plasma to yield $^{56}Fe^+/^{24}Mg^+$ up to 2.0 resulted in no shifts in $^{25}Mg/^{24}Mg$ and $^{26}Mg/^{24}Mg$ (Table 2). In this study measured $^{56}Fe^+/^{24}Mg^+$ values were always <2.0, measured $(^{23}Na^+ + ^{46}Ca^{++})/^{24}Mg^+$ (i.e., the measured 23/24 m/z) were all ≪ 0.1 with the exception of analyses of JL-1 clinopyroxene for which the ratios were ≤ 0.4, and measured $^{27}Al^+/^{24}Mg^+$ were all ≪1.0 with the exception of the CAI data for which

Table 4. Laser ablation analyses of USNM 136718 forsterite with and without Na added to the plasma source of the MC–ICPMS instrument. Concentrations refer to Na in 2% nitric acid solution aspirated through the desolvating nebulizer during ablation. Values in column 2 are as measured.

Run No. and sample	$^{23}Na^+/^{24}Mg^+$	$\delta^{25}Mg_{SRM\ 980}$	$\delta^{26}Mg_{SRM\ 980}$
2919 USNM 136718	0.00	1.55	3.05
2920 USNM 136718 + 1.0 ppm Na	0.33	1.62	3.14
2921 USNM 136718	0.00	1.70	3.29
2922 USNM 136718 + 1.0 ppm Na	0.36	1.88	3.58
2923 USNM 136718	0.00	1.78	3.48
2924 USNM 136718 + 1.0 ppm Na	0.34	1.69	3.29
2925 USNM 136718	0.00	1.71	3.37
2926 USNM 136718 + 1.0 ppm Na	0.36	1.62	3.11
Mean with no Na added	**0.00**	**1.68 +/− 0.20 (2σ)**	**3.30 +/− 0.37 (2σ)**
Mean with Na added	**0.35**	**1.70 +/− 0.24 (2σ)**	**3.28 +/− 0.43 (2σ)**

Table 5. Laser ablation analyses of USNM 136718 forsterite with and without Ca added to the plasma source of the MC–ICPMS instrument. Concentrations refer to Ca in 2% nitric acid solution aspirated through the desolvating nebulizer during ablation. Values in column 2 are as measured.

Run No. and sample	$^{44}Ca^{++}/^{24}Mg^{+}$	$\delta^{25}Mg_{SRM\ 980}$	$\delta^{26}Mg_{SRM\ 980}$	$\Delta^{25}Mg_{TMF}$[†]
2989 USNM 136718	0.00	1.75	3.33	0.02
2990 USNM 136718	0.00	1.71	3.29	0.00
2991 USNM 136718	0.00	1.69	3.17	0.05
2994 USNM 136718 + 48 ppm Ca	2.6×10^{-3}	1.50	3.01	−0.05
2995 USNM 136718	0.00	1.71	3.22	0.05
2997 USNM 136718 + 88 ppm Ca	4.3×10^{-3}	1.15	2.63	−0.21
2998 USNM 136718 + 160 ppm Ca	7.7×10^{-3}	0.75	1.93	−0.25
2999 USNM 136718	0.00	1.74	3.15	0.11
3061 USNM 136718 + ~200 ppm Ca	14.6×10^{-3}	0.02	1.44	−0.73

[†] $\Delta^{25}Mg = \delta^{25}Mg - 0.52\ \delta^{26}Mg$ where 0.52 is the slope of the terrestrial mass fractionation line defined by acid digestion MC–ICPMS measurements of terrestrial samples (Galy et al., 2001).

values were as high as 4.7 (see below). Comparison of these measured ratios with the values in Tables 2–4 suggests that the measured Mg isotope ratios were not affected by Fe, Al, and Na released from the samples during laser ablation.

The difference in Mg isotope ratios between mantle clinopyroxene and olivine obtained by laser ablation matches that obtained when Mg is chemically isolated from these samples (Table 1). JL-1 cpx yields $^{44}Ca^{++}/^{24}Mg^{+}$ of 1.3×10^{-3} compared with 0.000 for JL-1 ol, suggesting that the disparate chemical compositions of these two phases do not influence measured isotope ratios.

The reason that mass fractionation of the Mg isotopes was observed in some of our Ca doping experiments (Fig. 2) while no mass fractionation was observed in our Na, Al, and Fe doping experiments is apparently because the amounts of Ca added to cause the mass fractionation are extreme in comparison to the concentrations of Ca, Na, Al, and Fe added in the other experiments (Tables 2–5).
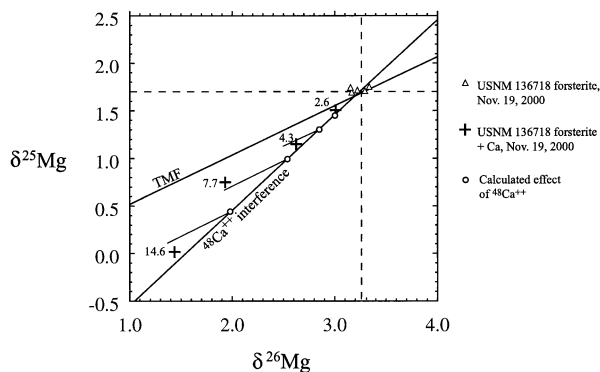

Fig. 2. Magnesium three-isotope plot (relative to the SRM 980 Mg standard) showing the effects of $^{48}Ca^{++}$ interference on $^{25}Mg/^{24}Mg$ and $^{26}Mg/^{24}Mg$ measured in USNM 136718 forsterite using laser ablation and MC–ICPMS. Crosses show measured values. Numbers adjacent crosses refer to measured $^{44}Ca^{++}/^{24}Mg^{+}$ multiplied by 10^3. Note that Ca causes spurious measurements of Mg isotope ratios when $^{44}Ca^{++}/^{24}Mg^{+}$ exceeds $\approx 1.0 \times 10^{-3}$ (i.e., where $^{48}Ca^{++}/^{24}Mg^{++}$ exceeds 9.0×10^{-5}). Open circles show the calculated effects of $^{48}Ca^{++}$ interference at $m/z = 24$. Comparison between measured and calculated interference effects suggests that abundant Ca in the source of the MC–ICPMS instrument causes mass-dependent shifts in Mg isotope ratios, shown by lines parallel to the terrestrial mass fractionation line (TMF), in addition to mass interference.

3.3. Laser Ablation Effects

Inspection of ultraviolet laser ablation pits by backscattered electron imaging, micro-Raman spectroscopy, and characteristic x-ray analysis in this study and in previous studies devoted to oxygen isotope ratio analysis has shown that extraction of the material from the laser pits is quantitative (i.e., the walls and floors of the pits are indistinguishable from the starting materials, see Young et al., 1998a, and references therein). If there is fractionation due to the laser sampling process then it must arise during condensation after ablation rather than as a result of the ablation itself. We have not undertaken a systematic study of the composition of the powder fallout that appears around each ablation pit, but our characteristic x-ray analyses of the powder that surrounds pits in the CAI (undertaken because we were concerned about Al loss) show it to be made almost entirely of a Ca compound that is most likely CaO (suggesting that it is a condensate and not a fine powder of starting material). We take the accuracy of our standard olivine and clinopyroxene measurements as evidence that Mg isotope fractionation due to condensation, if it occurs, is not significant. In addition, the fact that our chondrule and CAI Mg isotope data are consistent with previous measurements obtained by acid digestion (see below), and the fact that our measured Al/Mg ratios are consistent with characteristic x-ray analyses, indicates that laser sampling does not introduce a discernible bias to the data with the operating conditions used in this study.

4. SAMPLE DESCRIPTIONS

Four chondrules and a portion of a CAI from the Allende CV3 carbonaceous chondrite were sampled. Laser ablation oxygen isotope ratio data exist for each of the objects as part of previous studies (Young and Russell, 1998; Ash et al., 1999; Young et al., 1999). Most of the chondrule oxygen data have until now only appeared in graphical form. The data are summarized here in Table 6 and in Fig. 3. The CAI oxygen isotope data were described in detail by Young and Russell (1998).

4.1. Chondrule C6

Allende C6 is a coarse-grained barred olivine chondrule with a devitrified mesostasis consisting of albitic feldspar and enstatite. Pyroxene is the dominant mineral along much of the outer margin. The chondrule weighed 29.23 mg prior to sam-

Table 6. Laser ablation oxygen isotope ratio data for Allende chondrules C6, C8, C9, and C13 for which laser ablation Mg isotope ratio data were collected as part of this study and chondrules A3, A4, A5, A6, and A7 for which bulk Mg isotope data exist.

Sample, spot No.	Mineralogy[¶]	$\delta^{17}O^{SMOW}_{\dagger}$	$\delta^{18}O^{SMOW}_{\dagger}$	$\Delta^{17}O^{\ddagger}_{TMF}$
C6, 4	px, margin	−2.1	1.3	−2.8
C6, 5	mes > ob	−1.5	2.2	−2.6
C6, 6	ob	−2.5	1.3	−3.2
C6, 7	ob, margin	−2.4	0.6	−2.7
C6, 8	ob > mes	−1.4	2.1	−2.5
C6, 9	mes ≫ ob	−0.9	3.3	−2.6
C6, 11	ob	−2.4	0.9	−2.8
C6, 12	mes	−1.6	2.7	−2.9
C6, 13	ob, margin	−2.1	1.0	−2.6
C6, 14	px, margin	−2.3	1.1	−2.9
C6, 15	px ≫ mes, margin	−1.7	1.4	−2.4
C6, 16	ob	−2.3	1.1	−2.8
C6, 17	mes	−1.2	3.0	−2.8
C6, 18	mes > ob	−1.8	2.3	−3.0
C8, 1	alt + fo + mes	−3.5	0.9	−3.9
C8, 2	fo + mes	−11.8	−8.9	−7.2
C8, 3	alt + fo + mes	−2.7	1.6	−3.5
C8, 4	fo + mes	−10.9	−7.2	−7.2
C8, 5	alt + fo + mes	−5.0	−1.0	−4.5
C8, 6	alt + fo + mes	−4.2	−0.6	−3.9
C8, 7	alt < fo + mes	−6.7	−2.1	−5.6
C8, 8	Alt < fo + mes	−7.0	−3.4	−5.2
C9, 4	px	−2.6	0.2	−2.7
C9, 5	px	−2.5	0.5	−2.8
C9, 6	alt + mes	−2.1	1.5	−2.9
C9, 7	alt + px, margin	−1.5	2.3	−2.7
C9, 8	px	−2.6	0.8	−3.0
C9, 9	px ≫ alt, margin	−2.3	1.4	−3.0
C9, 10	alt + px, margin	−1.4	2.6	−2.8
C9, 11	px	−2.4	0.6	−2.7
C9, 12	alt + mes	−0.9	3.1	−2.5
C9, 13	px	−2.6	0.3	−2.8
C9, 14	ol + px	−2.5	1.3	−3.2
C9, 15	px	−2.4	0.9	−2.9
C13, 3	ob + mes, margin	−0.9	1.9	−1.9
C13, 5	ob + mes, center	−1.7	1.0	−2.2
C13, 6	ob + mes, margin	−2.7	0.2	−2.8
C13, 7	ob + mes, margin	−2.1	0.8	−2.5
C13, 8	ol + mes + alt	−1.2	1.7	−2.1
C13, 12	ol+mes+alt, margin	−1.5	1.4	−2.2
C13, 13	ol+mes+alt, margin	−1.5	1.3	−2.1
A3, 3	px, margin	−2.5	0.0	−2.5
A3, 4	ol, core	−5.0	−3.0	−3.4
A3, 5	px, margin	−2.4	0.4	−2.6
A3, 8	ol, core	−3.7	−1.0	−3.2
A3, 9	ol, core	−3.7	−1.3	−3.0
A3, 10	px, margin	−3.0	0.5	−3.2
A3, 11	px, margin	−2.9	0.6	−3.2
A3, 11-1	ol, core	−4.9	−3.3	−3.2
A3, 12	ol, core	−3.2	−1.8	−2.3
A3, 13	px, margin	−2.3	0.2	−2.4
A3, 14	ol, core	−4.2	−2.5	−2.9
A3, 15	px, margin	−2.6	0.8	−3.0
A3, 16	ol, core	−4.1	−2.8	−2.7
A3, 17	px, margin	−2.2	1.5	−3.0
A4, 1	px+feld+sp	−9.7	−6.1	−6.5
A4, 2	alt+px+feld+sp	−8.1	−4.5	−5.7
A4, 3	px+feld+sp	−9.2	−6.2	−6.0

(Continued)

Table 6. (Continued)

Sample, spot No.	Mineralogy[¶]	$\delta^{17}O^{SMOW}_{\dagger}$	$\delta^{18}O^{SMOW}_{\dagger}$	$\Delta^{17}O^{\ddagger}_{TMF}$
A5, 1	px+fo	−5.3	−1.5	−4.5
A5, 2	alt+px+fo+mes	−4.2	−0.4	−4.0
A5, 3	Alt+px+fo+mes	−3.9	−0.8	−3.5
A5, 4	px+fo	−5.6	−2.6	−4.3
A6, 2	fo+mgt, core	−4.6	−1.5	−3.8
A6, 3	fo+alt, rim	−2.8	1.0	−3.4
A6, 4	fo+mgt, core	−6.2	−3.3	−4.5
A6, 5	fo+alt, rim	−3.6	0.1	−3.7
A6, 6	fo+mgt, rim	−5.9	−3.1	−4.3
A6, 7	fo+alt, rim	−3.9	0.0	−3.9
A6, 8	fo+mgt, core	−4.1	−0.4	−3.9
A6, 9	fo+mgt, core	−7.4	−4.9	−4.8
A6, 10	fo+alt, rim	−3.5	0.5	−3.8
A7, 2	ob	−2.6	0.7	−2.9
A7, 3	alt+mes	0.0	5.1	−2.7
A7, 4	mes	−2.0	0.9	−2.4

[¶] px = pyroxene, mes = mesostasis, ol = olivine, ob = olivine bar, fo = relict forsterite, feld = feldspar, alt = alteration, mgt = magnetite.

[†] Precision for $\delta^{17}O$ and $\delta^{18}O$ is +/− 0.2 and +/− 0.3‰ (1σ), respectively. Data collected with method described by Young et al. (1998a).

[‡] $\Delta^{17}O = \delta^{17}O - 0.52\ \delta^{18}O$, per mil deviations in $^{17}O/^{16}O$ from the terrestrial mass fractionation line in three-isotope space.
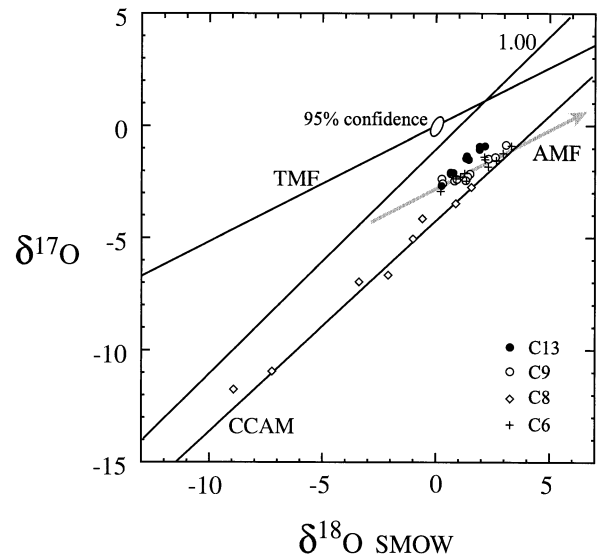

Fig. 3. Oxygen three-isotope plot (relative to SMOW) showing UV laser ablation data for the chondrules analyzed as part of this study. Notice that data for C6 and C9 lie on the Allende mass fractionation line (AMF) delineated with the grey arrow that parallels the terrestrial mass fractionation line (TMF). Chondrule C8 shows large excesses in ^{16}O that correlate with the presence of relict forsterite grains. Higher $\delta^{18}O$ values correspond to altered areas in each of the chondrules. Error ellipse represents the 95% confidence interval determined by the eigenvectors and eigenvalues for the variances and covariances in $\delta^{17}O$ and $\delta^{18}O$ for standards (The correlation coefficient for $\delta^{17}O$ and $\delta^{18}O$ is 0.46 when measured by the method of Young et al., 1998a).
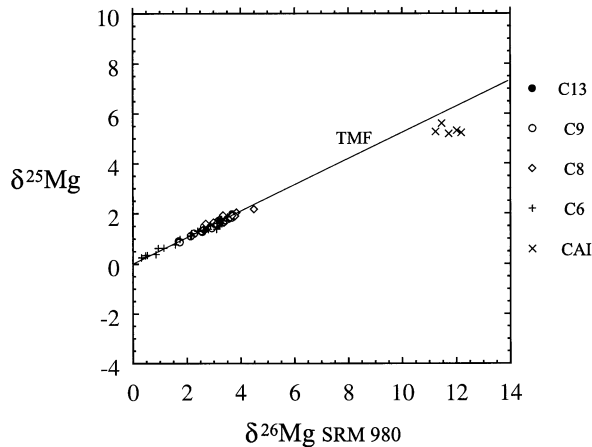
Fig. 4. Magnesium three-isotope plot (relative to the SRM 980 Mg standard) of UV laser ablation/ MC–ICPMS data for Allende chondrules and a CAI from Allende. The chondrule data lie on the terrestrial mass fractionation line (TMF) with a slope of 0.52. The CAI data deviate from this line due to the presence of radiogenic ^{26}Mg.

pling. Enrichments in Cl and Fe at the edges of the chondrule and in the mesostasis are manifestations of alteration on a fine scale.

Mineral oxygen isotope ratios from C6 lie on a mass fractionation line on the oxygen three isotope plot (Fig. 3, abscissa = δ^{18}O relative to SMOW, ordinate = δ^{17}O relative to SMOW) with a mean Δ^{17}O of -2.75 ‰ (Δ^{17}O = δ^{17}O $- 0.52$ δ^{18}O and is the per mil deviation from the terrestrial mass fractionation line along the ordinate of the three isotope plot). The fractionation line is referred to as the AMF (Allende Mass Fractionation line, Young et al., 1999; see also Ash et al., 1999). Olivine bars and marginal pyroxene exhibit a range in δ^{18}O ($+/-0.3$ ‰) values from $+0.6$ to $+1.4$ ‰. Mesostasis δ^{18}O ranges from 2.2 to 3.3 ‰. The difference in oxygen isotopic composition between olivine and mesostasis has been attributed to alteration concentrated in the latter in view of the high temperatures attending chondrule crystallization (Young et al., 1999; Ash et al., 1999).

4.2. Chondrule C8

Allende C8 is a porphyritic olivine chondrule that weighed 13.88 mg prior to sampling. Most olivine grains are forsterite (Fo>99) and range in diameter from 10 to 40 μm. The forsterite grains are similar to grains identified in previous studies as relicts that predate the formation of their host chondrules (Weinbruch et al., 2000); they are too Mg-rich to have grown from the chondrule melt. Forsterites are surrounded by a fine-grained mixture of pyroxene and feldspar. Some regions of the chondrule have been altered as evidenced by leach holes and enrichments in Fe, Cl, and Na. Olivines in the altered areas have Fe-rich rims but are otherwise identical to the relict forsterites in crystal habit and abundance.

Oxygen isotope ratios obtained by laser ablation of C8 lie along the carbonaceous chondrite anhydrous mineral line (CCAM) with a slope of approximately 0.94 on the oxygen three isotope plot (Fig. 3, Ash et al., 1999). Values for δ^{18}O range from -8.9 to $+1.6$ ‰. Each oxygen isotope analysis is

composed of a mixture of forsterite and pyroxene/feldspar mesostasis. The position of each datum along the CCAM correlates with the amount of alteration sampled by the laser, with the most altered samples having the highest Δ^{17}O values and the least altered samples (e.g., dominantly forsterite) having the lowest Δ^{17}O values (Ash et al., 1999).

4.3. Chondrule C9

Allende C9 is a porphyritic pyroxene olivine chondrule with coarse-grained pyroxene poikilitically enclosing olivine. Pyroxenes are typically 0.5 to 1.0 mm in diameter. The olivine chadacrysts range from 20 to 90 μm in diameter and are relatively rich in Fe. The chondrule weighed 36.93 mg prior to sampling. Devitrified mesostasis surrounding the pyroxene is Fe, Cl, and Na rich, indicating that it has been altered. Enrichment in Fe is also evident along the edge, suggesting that alteration was most pronounced in the outer portions of the chondrule.

Oxygen isotope ratios are similar to those of chondrule C6 (Fig. 3) with compositions along the AMF, a range in pyroxene δ^{18}O from $+0.2$ to $+1.4$ ‰, and a range in mesostasis δ^{18}O from $+1.5$ to $+3.1$ ‰ (Fig. 3). Laser ablation samples of the altered Fe-rich edge of the chondrule yield δ^{18}O values of between $+2.3$ and $+2.6$ ‰ while the highest value of 3.1‰ also comes from an altered area.

4.4. Chondrule C13

Allende C13 is a fine-grained barred olivine chondrule. Olivine bars are 10 to 15 μm wide. The chondrule weighed 4.88 mg prior to sampling. Its small grain size prevented mineral-specific oxygen isotope ratio analysis despite laser sampling. Oxygen isotope analyses of this chondrule comprise mixtures of bars and mesostasis with variable degrees of alteration. The data define a slope-1 line on the oxygen three isotope plot (Fig. 3, Ash et al., 1999). One end of the slope-1 line corresponds to values that characterize unaltered olivine and pyroxene in C6 and C9. The other end extends toward the field of Allende barred chondrules defined by Clayton et al., 1983).

4.5. CAIUSNM 3576-1

USNM 3576-1 is a coarse-grained type B CAI that measured 2 cm by 0.5 cm before sampling. It consists mainly of melilite and Al- and Ti-rich pyroxene (fassaite). Spinel occurs as ubiquitous inclusions and is most abundant in fassaite. The åkermanite content of the melilite decreases systematically from the interior to the margin of the CAI. Feldspar (An$_{99-100}$) is also present and is most abundant adjacent fassaite. Alteration characterized by alkali and halogen element enrichments is concentrated at the outer margins of the CAI and around fassaite. Altered areas exhibit higher δ^{18}O values than unaltered areas at equivalent Δ^{17}O as a result of mass-dependent increases in oxygen isotope ratios (Young and Russell, 1998; Young et al., 1999). A more complete description of the CAI together with a detailed discussion of the laser ablation oxygen isotope data obtained from it was presented by Young and Russell (1998).

Table 7. Laser ablation MC–ICPMS magnesium isotope ratio data for Allende chondrules C6, C8, C9, and C13.

Sample, spot No.	$\delta^{25}Mg_{SRM\ 980}$	$\delta^{26}Mg_{SRM\ 980}$	$\Delta^{25}Mg_{TMF}$[†]
C6, 8	1.2	2.2	0.06
C6, 9	1.7	3.5	−0.10
C6, 10	1.4	2.8	−0.06
C6, 11	1.4	3.1	−0.21
C6, 12	1.6	3.1	−0.01
C6, 13	1.5	3.2	−0.16
C6, 14	1.6	2.9	0.09
C6, 15	0.6	1.2	−0.02
C6, 16	1.3	2.6	−0.05
C6, 17	0.6	0.9	0.13
C6, 18	0.3	0.5	0.04
C6, 19	1.8	3.3	0.08
C6, 20	0.3	0.3	0.14
C6, 21	0.8	1.6	−0.03
C6, 22	1.1	2.1	0.01
C6, 23	1.1	2.2	−0.04
C6, 24	1.0	1.8	0.06
C6, 25	1.7	3.3	−0.02
C6, 26	1.9	3.5	0.08
C6, 27	0.4	0.5	0.14
C6, 28	0.4	0.9	−0.07
C6, 29	1.3	2.6	−0.05
C6, 30	1.6	3.3	−0.12
C6, 31	1.3	2.4	0.05
C6, 32	1.3	2.4	0.05
C6, 33	1.6	3.1	0.01
C8, 1	1.9	3.7	0.02
C8, 2	2.0	3.8	0.05
C8, 3	2.2	4.5	−0.16
C8, 4	1.8	3.4	0.05
C8, 5	1.7	3.1	0.07
C8, 6	1.4	2.6	0.05
C8, 7	1.7	3.0	0.14
C8, 8	1.7	3.4	−0.05
C8, 9	1.8	3.3	0.08
C8, 10	1.5	3.1	−0.11
C8, 11	1.7	3.3	−0.02
C8, 12	1.7	3.3	−0.02
C8, 13	1.8	3.4	0.03
C8, 14	1.9	3.7	−0.06
C8, 15	1.6	2.7	0.20
C8, 16	1.6	3.1	−0.02
C8, 17	1.8	3.6	−0.03
C8, 18	1.6	3.4	−0.17
C8, 19	1.9	3.8	−0.06
C8, 20	1.7	3.4	−0.07
C8, 21	1.9	3.7	−0.02
C8, 22	1.9	3.3	0.20
C9, 1	1.8	3.7	−0.12
C9, 2	1.5	3.0	−0.06
C9, 3	1.4	2.9	−0.11
C9, 4	1.4	2.7	0.00
C9, 5	1.2	2.3	0.00
C9, 6	0.9	1.7	0.02
C9, 7	1.6	3.1	−0.01
C9, 8	1.1	2.1	0.00
C9, 9	0.9	1.7	0.02
C9, 10	1.5	2.6	0.15
C9, 11	1.3	2.6	−0.05
C9, 12	1.8	3.3	0.08
C9, 13	1.3	2.6	−0.05
C9, 14	1.6	3.0	0.04
			(Continued)

Table 7. (Continued)

Sample, spot No.	$\delta^{25}Mg_{SRM\ 980}$	$\delta^{26}Mg_{SRM\ 980}$	$\Delta^{25}Mg_{TMF}$[†]
C13, 1	1.7	3.3	−0.02
C13, 2	1.7	3.3	−0.02
C13, 3	1.7	3.3	−0.02
C13, 4	1.7	3.2	0.04
C13, 5	1.8	3.5	−0.02
C13, 6	2.0	3.7	0.08
C13, 7	1.8	3.5	−0.02
C13, 8	1.7	3.2	0.04
C13, 9	1.6	3.1	−0.01

[†] $\Delta^{25}Mg = \delta^{25}Mg - 0.52\ \delta^{26}Mg$ where 0.52 is the slope of the terrestrial mass fractionation line defined by acid digestion MC–ICPMS measurements of terrestrial samples (Galy et al., 2001).

RESULTS

All of the laser ablation Mg isotope data for Allende are plotted in Fig. 4 and listed in Tables 7 and 8. The mineralogy of the spot analyses can be seen in the backscattered electron images shown in Figs. 5–9. Chondrule analyses define an array of mass-dependent variations in $\delta^{25}Mg$ and $\delta^{26}Mg$ indistinguishable from the terrestrial mass fractionation line (Fig. 4). The CAI data fall to the right of the terrestrial mass fractionation line (Fig. 4).

5.1. Chondrule C6

Chondrule C6 has relatively uniform $^{25}Mg/^{24}Mg$ and $^{26}Mg/^{24}Mg$ throughout most of its interior with $\delta^{25}Mg$ values of 1.9 to 1.7 ‰. At the margins $\delta^{25}Mg$ is significantly lower than in the interior with values ranging down to 0.3‰ (Fig. 5). The low $\delta^{25}Mg$ values occur in both olivine and pyroxene at the margins. Conversely, oxygen isotope ratios in olivine and pyroxene are relatively uniform throughout the chondrule (Fig. 5) with $\delta^{18}O$ values between 0.6 and 1.4 ‰. Higher $\delta^{18}O$ values occur in the mesostasis where alteration is most pronounced. Ferromagnesian phases in C6 show a systematic zonation in Mg isotope ratios of 1.5‰ per amu while at the same time relative uniformity in O isotope ratios with variations of only 0.4‰ per amu.

5.2. Chondrule C8

Chondrule C8 has more uniform $\delta^{25}Mg$ than C6. In C8 there is a correlation between the presence of relict refractory grains of forsterite, low $\Delta^{17}O$, and high $\delta^{25}Mg$ (Fig. 6). Inside unaltered regions rich in relict olivines $\delta^{25}Mg$ averages 1.9 ‰ +/− 0.2 (2σ) and $\Delta^{17}O$ is −7.2‰. Outside the unaltered relict-rich regions mean $\delta^{25}Mg$ is 1.6 ‰ +/−0.2 (2σ) and mean $\Delta^{17}O$ is −4.4‰ +/−1.6 (2σ). Alteration coincides with higher $\Delta^{17}O$ and lower $\delta^{25}Mg$ in C8.

5.3. Chondrule C9

Chondrule C9 is similar to C6 in that it belongs to the group of chondrules with $\Delta^{17}O$ values on the Allende mass fractionation line (Fig. 3). The Mg isotope data are also similar to those for C6 in that $\delta^{25}Mg$ decreases systematically from a maximum of 1.8‰ in the interior to a minimum of 0.9‰ at the margins

Table 8. Laser ablation MC–ICPMS Mg and Al isotope ratio data for Allende CAI USNM 3576-1. Mg isotope ratios are reported relative to the SRM 980 standard.

Spot No.	Minerals[¶]	$\delta^{25}Mg$	$\delta^{26}Mg$	$\Delta^{25}Mg_{TMF}$	$\delta^{26}Mg*^{†}$	$^{27}Al/^{24}Mg$	$^{44}Ca^{++}/^{24}Mg^{+‡}$
1	fs+sp+alt	5.6	11.5	−0.37	0.69	2.67	5.3×10^{-4}
2	mel	5.2	11.7	−0.86	1.74	3.29	4.3×10^{-4}
3	mel	5.3	12.0	−0.92	1.79	4.00	1.1×10^{-3}
4	fs+sp	5.3	11.2	−0.52	1.10	2.65	2.2×10^{-4}
5	mel	5.2	12.2	−1.14	2.13	4.72	9.3×10^{-4}

[¶] fs = fassaite, sp = spinel, alt = alteration.
[†] $\delta^{26}Mg* = \delta^{26}Mg - \delta^{25}Mg/0.52$ where 0.52 is the slope of the terrestrial mass fractionation line defined by acid digestion MC–ICPMS measurements of terrestrial samples (Galy et al., 2001).
[‡] As measured. Values $\leq 1 \times 10^{-3}$ ensure that Ca interference effects are less than 0.09‰ (cf. Table 5).

(Fig. 7). Alteration is concentrated near the rim in this chondrule, suggesting that the lower $\delta^{25}Mg$ values are related to the alteration.

5.4. Chondrule C13

C13 shows virtually no variation in Mg isotope ratios with a mean $\delta^{25}Mg$ of 1.7‰ +/−0.2 (2σ) (Fig. 8). Oxygen isotope ratios in C13 are relatively uniform with the exception of a spread in $\Delta^{17}O$ of 0.9‰ (Fig. 8). It is possible that this apparent homogeneity in isotopic composition is a result of a small grain size in comparison with the size of the laser ablation pits.

However, two analyses at the outer edge of the chondrule are identical to the analyses in the interior, suggesting that zoning in $\delta^{25}Mg$ like that seen in the other chondrules is absent in this object.

5.5. CAI USNM 3576-1

Five laser ablation pits were analyzed in USNM 3576-1 [Fig. 9(a)]. Three of the pits (spots 2, 3, and 5) sampled melilite with small amounts of included spinel. Another (spot 4) sampled fassaite with abundant spinel inclusions. The remaining pit
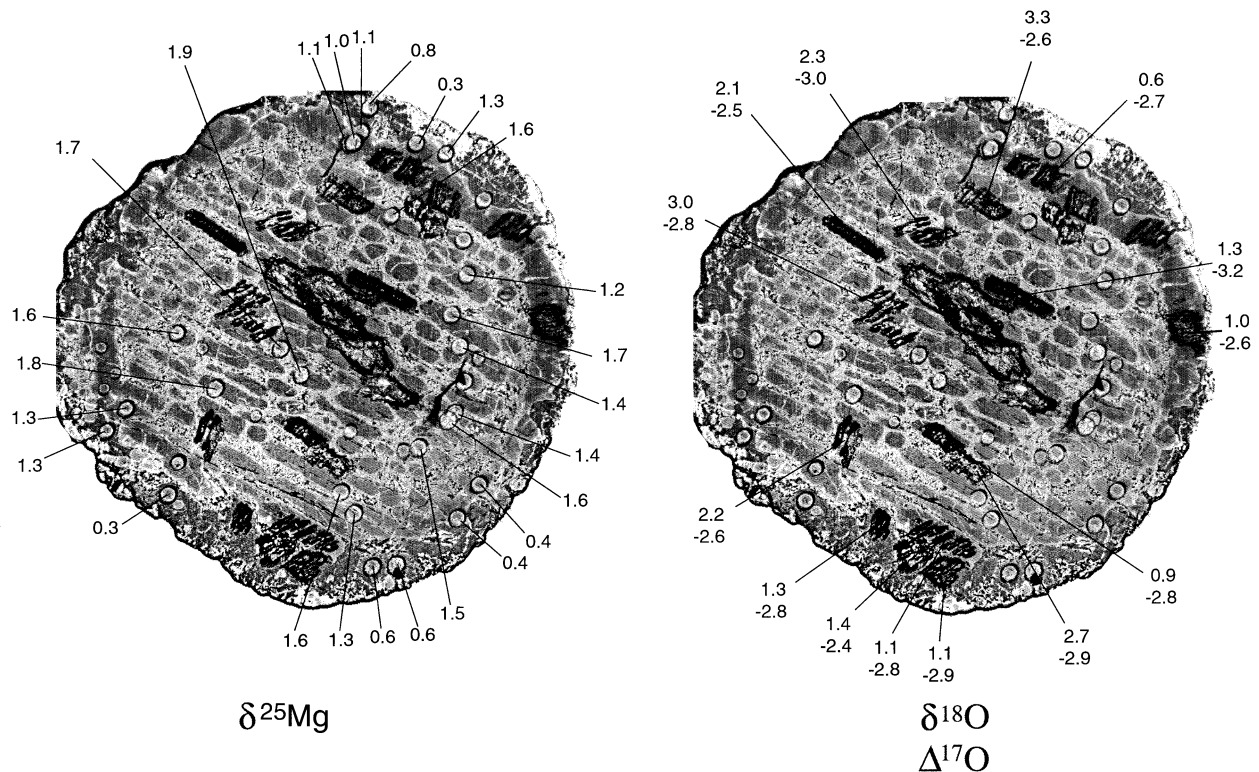

Fig. 5. Backscattered electron images of chondrule C6. The left image shows the UV laser ablation pits made during Mg isotope ratio analysis (circular pits 100 μm in diameter) and their corresponding $\delta^{25}Mg$ values. The image on the right correlates the UV laser pits from which O isotope data were obtained with the $\delta^{18}O$ and $\Delta^{17}O$ values for these pits. The O pits were made by rastoring a 20 μm UV laser beam. Darkest areas around the margins are pyroxene. Olivine bars appears as medium grey. Bright mottled areas are altered mesostasis interstitial to the bars.
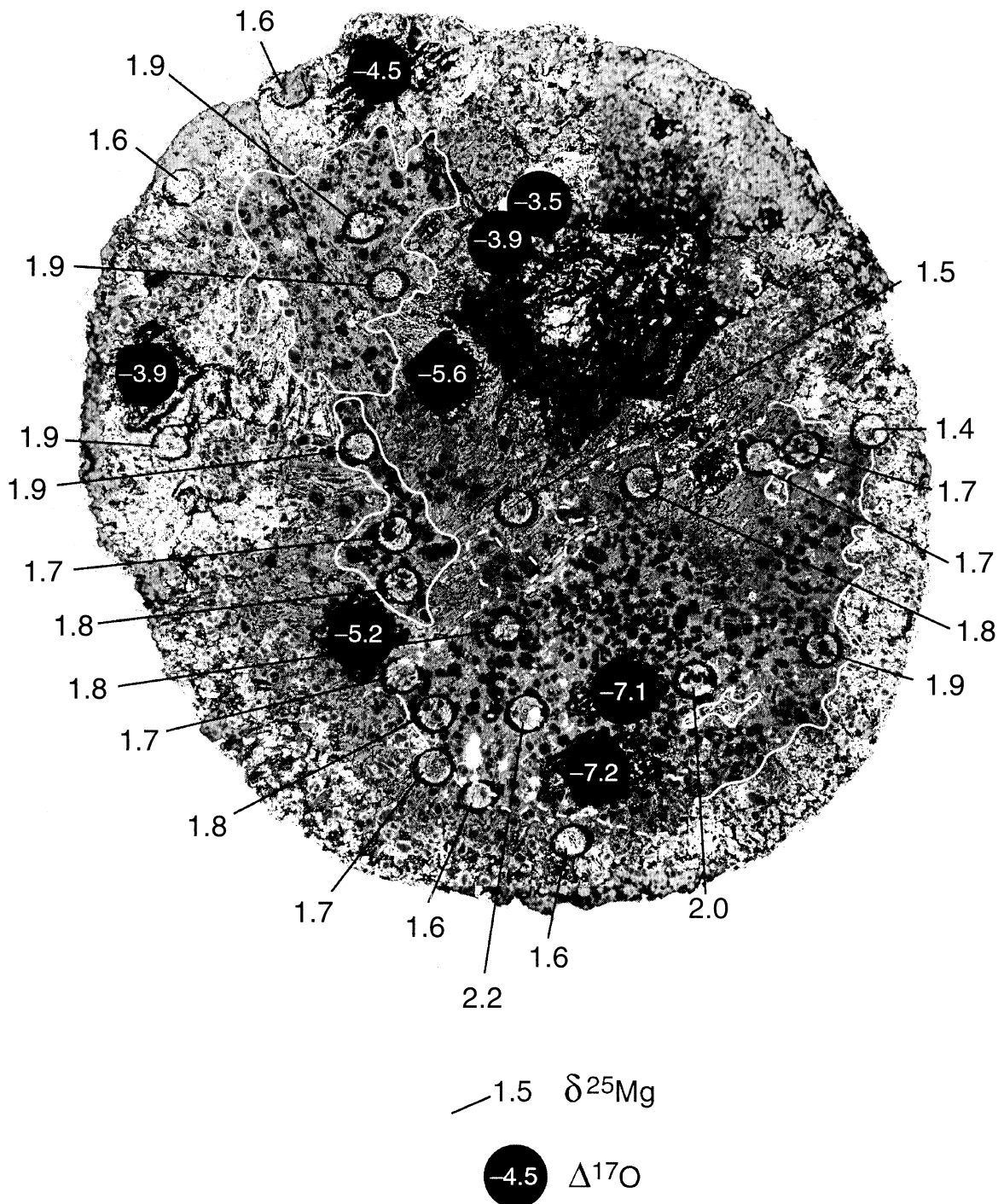
Fig. 6. Backscattered electron image of chondrule C8. Mg laser pits are circular and 100 μm in diameter. Oxygen laser pits (largely polished away) are marked by black circles. Relict forsterite appears as black crystals < 100 μm in diameter. Altered mesostasis is bright and mottled while unaltered mesostasis is medium grey. Highly altered areas appear white and mottled. The white line delimits regions relatively free of alteration and rich in relict forsterite grains. Note high δ^{25}Mg and low Δ^{17}O in these regions relative to the more altered areas outside the white line.

(spot 1) sampled mainly fassaite and spinel inclusions but intersected an area of alteration between two fassaite grains and two anorthite grains [Fig. 9(b)]. The alteration in this area is typical of fassaite–anorthite grain boundaries.

Laser spots 2, 3, 4, and 5 have the same ^{25}Mg/^{24}Mg ratio within analytical uncertainties (Fig. 10) with a mean δ^{25}Mg value of 5.3‰ +/−0.1 (2σ). These same laser samples vary in δ^{26}Mg by 1‰ (Fig. 10). Spot 1 includes the alteration at the
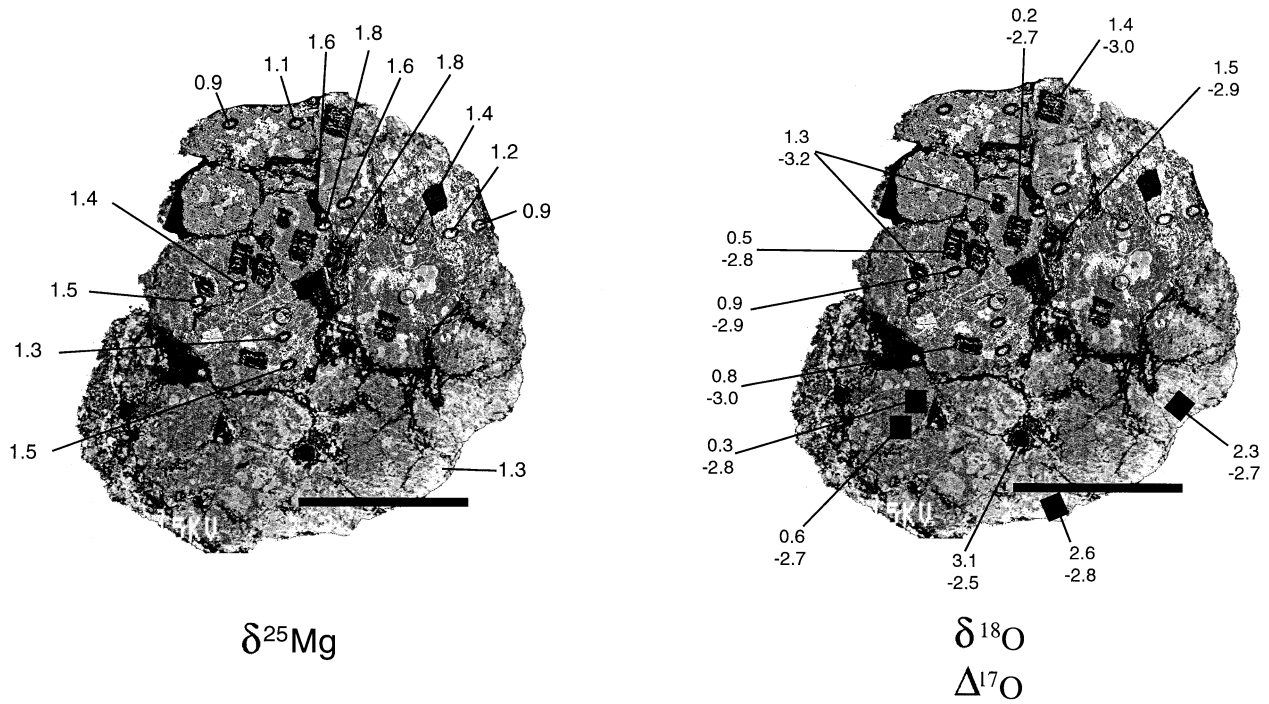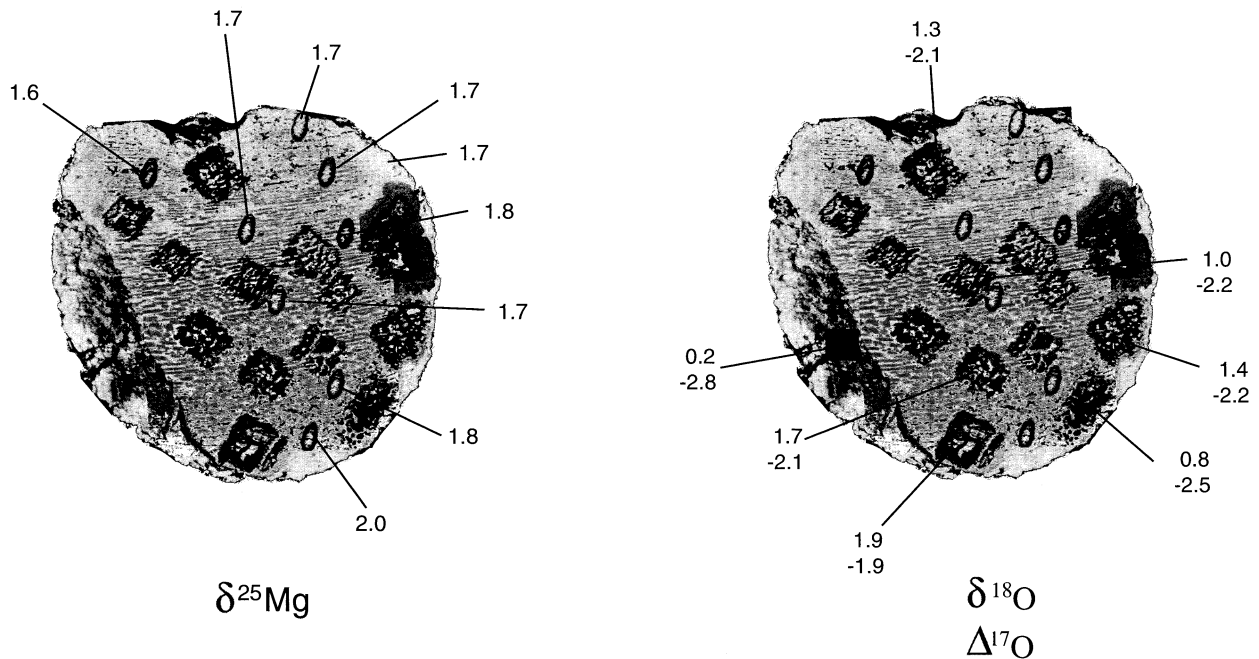
Fig. 7. Backscattered electron image of chondrule C9. Left image shows Mg laser pits together with $\delta^{25}Mg$ values for each pit. The pits are ovoid and 100 μm in their longest dimension. Right image correlates the O laser pits with the $\delta^{18}O$ and $\Delta^{17}O$ values for these pits. Four of the pits were polished away after analysis and are marked with black squares. Pyroxene is medium grey while altered areas are white and mottled. Note heavy alteration concentrated at the margins and the low $\delta^{25}Mg$ and high $\delta^{18}O$ in these altered areas. Scale bar is 1 mm.

Fig. 8. Backscattered electron image of chondrule C13. Left image shows Mg laser pits together with $\delta^{25}Mg$ values for each pit. The pits are ovoid and 100 μm in their longest dimension. Right image correlates the O laser pits with the $\delta^{18}O$ and $\Delta^{17}O$ values for these pits. Olivine bars are medium grey. Mesostasis is light grey. More altered areas are brighter in tone (e.g., near top margin). Note the homogeneity in $\delta^{25}Mg$.
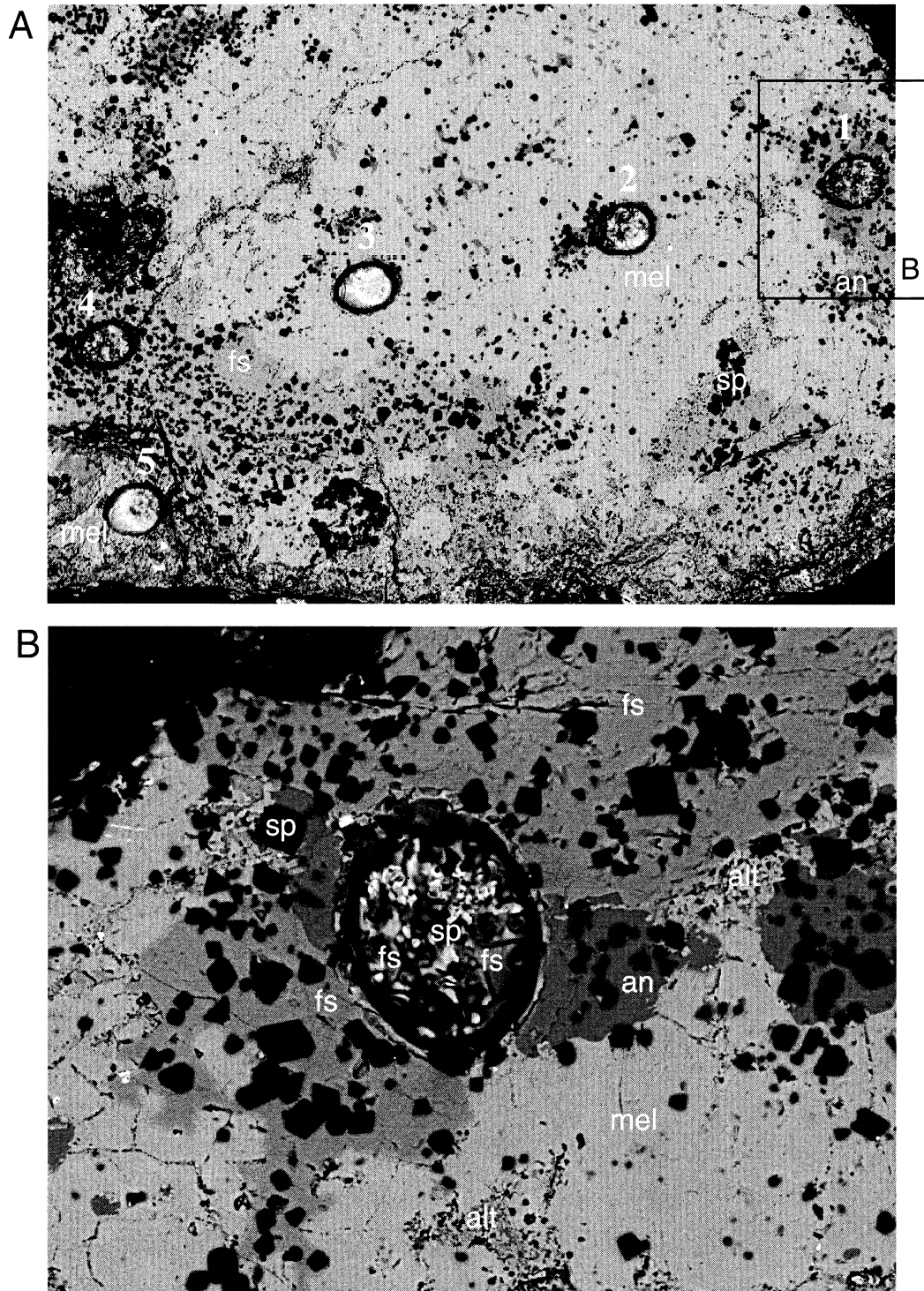
Fig. 9. (a) Backscattered electron image of Allende CAI USNM 3576-1 showing Mg laser ablation spots 1 through 5. Black crystals are spinel (sp), dark grey is anorthite (an), medium grey is fassaite (fs), and light grey is melilite (mel). (b) Close-up of sample spot No. 1 (rotated 90° ccw). Here the laser sampled fassaite between two crystals of anorthite. A band of alteration present between fassaite crystals was also ablated during this analysis. The alteration band is visible to the right side of the pit and appears as light and dark mottling in the upper half of the pit itself. Anorthite occurs on either side of the pit but no anorthite was found at the base of the pit and the Al/Mg ratio for this analysis indicates that the amount of anorthite sampled is negligible.
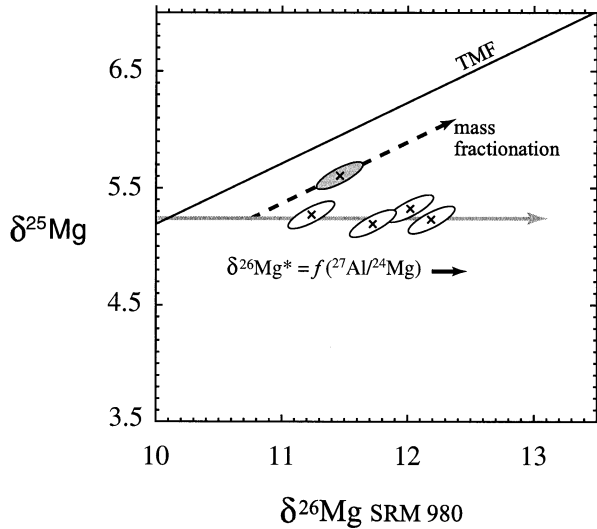
Fig. 10. Mg three-isotope plot showing laser ablation data for CAI USNM 3576-1. Ellipses represent the 95% confidence level calculated from the eigenvectors and eigenvalues derived from the variances and covariances of replicate analyses of USNM 136718 forsterite. The shaded datum is for spot No. 1 that includes alteration near the edge of fassaite. Note that this point has a different δ^{25}Mg than the other four analyses. The dashed line shows the trajectory of mass-dependent fractionation of altered material at constant δ^{26}Mg* relative to the unaltered minerals in the CAI.

fassaite–anorthite grain boundaries and yields a higher δ^{25}Mg of 5.6‰.

6. DISCUSSION

6.1. Chondrules

Allende matrix and whole-rock samples as well as matrix and bulk samples of other carbonaceous and ordinary chondrites have δ^{25}Mg values of 1.6 ‰ +/−0.1 (Galy et al., 2000; Galy and O'Nions, 2000). The laser ablation Mg isotope data show that Allende chondrules have δ^{25}Mg values that deviate from this "canonical" chondritic value for two reasons. One is that alteration is associated with low ^{25}Mg/^{24}Mg relative to the matrix of the meteorite. The other is that portions of chondrules containing abundant relict grains of refractory olivine have high ^{25}Mg/^{24}Mg relative to matrix. There is no evidence for increases in ^{25}Mg/^{24}Mg and ^{26}Mg/^{24}Mg that should result when molten silicates volatilize, suggesting that these objects were not molten at the low pressures envisaged for the early solar nebula (<100 Pa, Wood and Morfill, 1988). High gas pressures suppress fractionation in the liquid either by enhancing the evaporation rate such that diffusion is limiting (probably not viable for silicate liquids, Young, 2000) or by allowing gas and liquid to approach equilibrium (Galy et al., 2000). The alternative that the chondrules were molten for too short a time to exhibit fractionation can be discounted on the basis of diffusion arguments. The extent of Mg isotope fractionation at the surface of an evaporating silicate liquid is large. A fractionation factor corresponding to an enrichment in δ^{25}Mg of 20‰ is expected based on a kinetic fractionation factor of $(24/25)^{1/2}$ (e.g., Davis et al., 1990; Young et al., 1998b). We
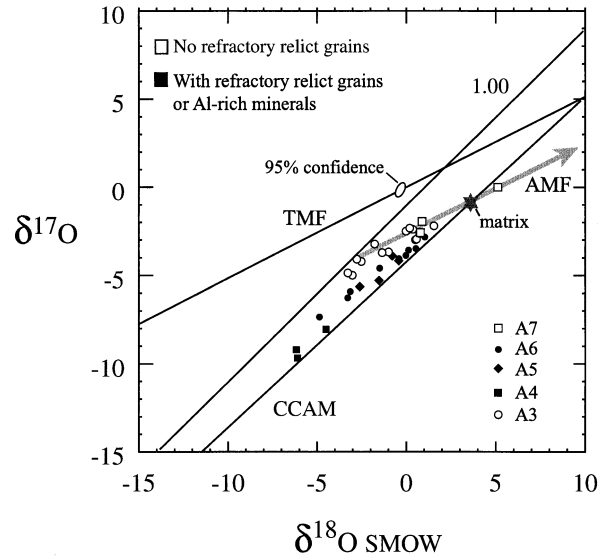

Fig. 11. Laser ablation O isotope ratio data for Allende chondrules A3, A4, A5, A6, and A7. The Allende mass fractionation line (AMF) is shown by the grey arrow parallel to the terrestrial mass fractionation line (TMF). Also shown are the carbonaceous chondrite anhydrous mineral line (CCAM) and the slope-1.00 line. Chondrules that lie below the AMF (black symbols) contain refractory components in the form of relict forsterite or in one case an Al-rich bulk composition (A4). Error ellipse represents the 95% confidence interval determined by the eigenvectors and eigenvalues for the variances and covariances in $\delta ^{17}$O and δ^{18}O for standards. (The correlation coefficient for $\delta ^{17}$O and δ^{18}O is 0.46 when measured by the method of Young et al., 1998a).

would expect to detect evaporative heavy isotope enrichment if the length scale for Mg diffusion was 50 μm or more from the edge of the chondrule. The diffusivity (D) of Mg in molten silicate is on the order of 1×10^{-9} to 5×10^{-9} m^2 s^{-1} (Young et al., 1998b) and the times obtained from the characteristic diffusive length scale, $z = (Dt)^{1/2}$, evaluated for $z = 50$ μm range from 2.5 to 0.5 s. A more rigorous calculation that includes the migration of the evaporating surface (Young et al., 1998b) shows that Mg isotope fractionation on the order of 5‰ per amu should develop in less than 30 s in a region extending tens of microns inward from the edges of the chondrules if they experienced free evaporation in the liquid state. This time scale is far shorter than that required for development of chondrule textures (chondrules are thought to crystallize on the time scale of many minutes to hours, Cohen et al., 2000) suggesting that a short interval above the solidus is not a realistic explanation for the lack of fractionation.

Alteration in chondrules C6 and C9 is concentrated at the margins where δ^{25}Mg values are low. In C8 the δ^{25}Mg values are not concentrically distributed, but low δ^{25}Mg values nevertheless occur where alteration is most pervasive, suggesting that it is the presence of alteration, rather than proximity to the edge of the chondrule, that determines the locations of low δ^{25}Mg values. Evaluation of the likelihood that low δ^{25}Mg values could be the result of aqueous alteration will require further studies of Mg isotope fractionation during low-T alteration of terrestrial rocks. An alternative explanation is that low δ^{25}Mg and alteration resulted from condensation (collision frequency of gaseous Mg is greater for the lighter isotopes).
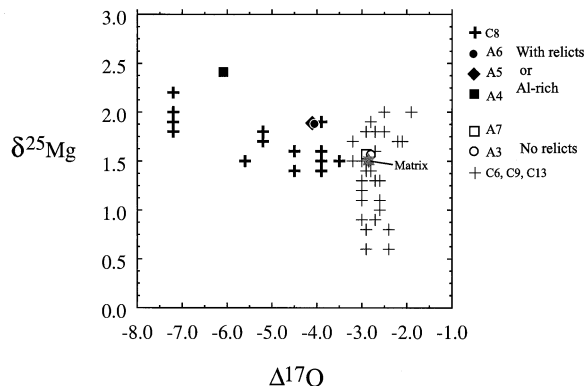
Fig. 12. Negative correlation between δ^{25}Mg and Δ^{17}O in Allende chondrules. Bulk δ^{25}Mg and average laser ablation Δ^{17}O values for chondrules A3, A4, A5, A6, and A7 are shown using the same symbols as in Fig. 11. Crosses are laser ablation data points constructed by correlating *in situ* δ^{25}Mg and Δ^{17}O measurements on the basis of mineralogy and texture. Heavy crosses are from chondrule C8 that contains relict forsterite. C8 should be compared with the forsterite-bearing chondrules A4 and A5, and the refractory Al-rich chondrule A6. Light crosses are from chondrules C6, C9, and C13 that have no relicts and are not Al rich. They should be compared with the relict-free and Al-poor chondrules A3 and A7. Grey star denotes the matrix composition of Allende. Based on these data it is concluded that inheritance influences both δ^{25}Mg and Δ^{17}O values in refractory-bearing chondrules while alteration controls δ^{25}Mg in chondrules with little or no refractory component.

Our previous studies of Allende chondrules (chondrules A3, A4, A5, A6, and A7, Ash et al., 2000; Galy et al., 2000) suggested that there is a negative correlation between bulk δ^{25}Mg and bulk Δ^{17}O in these objects. The laser ablation data presented here are consistent with this observation. The whole-chondrule data on which the correlation is based are shown in Figs. 11 and 12 and summarized in Table 9, and descriptions of the chondrules were given by Ash and Young (2000). Where there are only a few O isotope data points for a chondrule (e.g., A4), the laser pits were large in comparison to the entire object so that the average is representative of the object as a whole. Chondrules with forsterite that is likely relict like those in C8 (includes A5 and A6) have low Δ^{17}O and high δ^{25}Mg relative to the matrix of the meteorite. The Al-rich chondrule (A4) also has high δ^{25}Mg and low Δ^{17}O (Fig. 12), suggesting that it is refractory material in general that has high δ^{25}Mg and low Δ^{17}O.

There is no *a priori* method for combining the Mg and O laser ablation isotope data for comparison with the whole-chondrule data in Fig. 12 because the pits from the two studies do not coincide. Nevertheless, Mg and O isotope compositions can be paired on the basis of texture and mineralogy. Such pairings are plotted as crosses in Fig. 12 where it can be seen that low Δ^{17}O values in comparison to matrix (e.g., Δ^{17}O = −7.3 ‰ vs. the AMF where Δ^{17}O = −2.7‰) and high δ^{25}Mg values in comparison to matrix (e.g., δ^{25}Mg = 2.0 ‰ vs. the matrix value of 1.6 ‰, Fig. 12) are associated with relict olivine. The laser ablation data also demonstrate that the lowest δ^{25}Mg values in chondrules are associated with both alteration and Δ^{17}O values equivalent to the AMF (Fig. 12).

Overall the picture that emerges from the MC–ICPMS Mg isotope data is one of mixing between material with canonical

(matrix-like) Δ^{17}O and δ^{25}Mg and more refractory material with lower Δ^{17}O and higher δ^{25}Mg relative to matrix. In addition there are large variations in δ^{25}Mg at constant Δ^{17}O that correlate with degree of alteration.

6.2. CAI USNM 3576-1

In-situ measurements of both δ^{25}Mg and δ^{26}Mg with sub-per mil precision add a new dimension to studies of ^{26}Al–^{26}Mg systems in CAIs. The different δ^{25}Mg values between unaltered and altered material in USNM 3576-1 illustrate how mass-dependent fractionation can be used to determine the extent to which the CAI was closed to elemental transport, thus simplifying the interpretation of heterogeneity in ^{26}Mg excesses.

Uniformity in δ^{25}Mg among unaltered phases in CAI USNM 3576-1 is noteworthy because these high-precision analysis were obtained without normalization to a single ^{25}Mg/^{24}Mg value. A spread in δ^{26}Mg values at constant δ^{25}Mg among the low-Al minerals sampled by the laser, together with correlation between δ^{26}Mg* and ^{27}Al/^{24}Mg (Fig. 13), is clear indication that ^{26}Mg was added independently of ^{25}Mg by β^+ decay of ^{26}Al in these minerals (radiogenic ^{26}Mg = ^{26}Mg*). Analyses with the greatest Al and highest δ^{26}Mg* values in this study come from the gehlenitic melilite typical of the margin of the CAI.

Previous measurements of δ^{26}Mg* in CAIs were all made either by TIMS or SIMS. A uniform δ^{25}Mg is imposed on the TIMS data because the high-precision δ^{26}Mg* values are obtained by normalizing to a single "terrestrial" ^{25}Mg/^{24}Mg. The detection limit for δ^{26}Mg* by SIMS is sufficiently high that δ^{26}Mg* can only be detected with certainty in the most aluminous phases, including gehlenitic melilite (Al/Mg > 10), hibonite (Al/Mg > 15), and feldspar (Al/Mg > 200) (MacPherson et al., 1995; Sahijpal et al., 1998). The laser ablation MC–
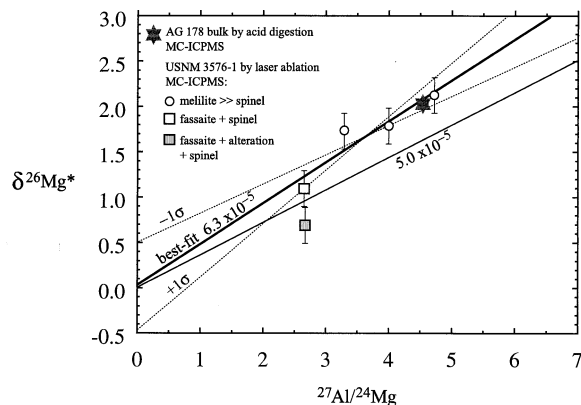

Fig. 13. ^{26}Al–^{26}Mg* evolution diagram for Allende CAI USNM 3576-1. Best-fit regression applies to the open data points representing material free from alteration. Dashed lines show the 1σ uncertainty in the regression. An MC–ICPMS whole-rock analysis of a different CAI from Allende (AG 178, grey star) and the canonical $(^{26}Al/^{27}Al)_o = 5 \times 10^{-5}$ line are shown for comparison. The uncertainty in the values for CAI AG 178 were reported by Galy et al. (2000) and are +/− 0.03 (2σ) for δ^{26}Mg* and +/− 0.1 for ^{27}Al/^{24}Mg (smaller than the symbol). Calculated $(^{26}Al/^{27}Al)_o$ derives from the equation $\delta^{26}Mg* = (^{26}Al/^{27}Al)_o (10^3/ (^{26}Mg/^{24}Mg)_{SRM\ 980}) (^{27}Al/^{24}Mg)$ and the value for $(^{26}Mg/^{24}Mg)_{SRM\ 980}$ of Catanzaro et al. (1966).

Table 9. Comparison of Mg isotope data for whole chondrules and averages of O isotope data for 5 Allende chondrules and whole-rock and matrix samples of Allende.

Sample	Type	Description[†]	$\Delta^{17}O_{TMF}$[††]	1σ	$^{27}Al/^{24}Mg$[‡]	$\delta^{25}Mg$[‡‡]	2σ
AG22	Whole rock*	$(n = 2)$			0.122	1.59	±0.03
AG23	Matrix*		-2.9^{12}		0.128	1.60	±0.01
A3	Chondrule	POP	-2.9 $(n=13)$	±0.4	0.078	1.63	±0.06
A4	Chondrule	Al rich	-6.1 $(n=3)$	±0.3	1.708	2.49	±0.07
A5	Chondrule	POP	-4.1 $(n=4)$	±0.4	0.334	1.97	±0.08
A6	Chondrule	PO	-4.1 $(n=8)$	±0.5	0.263	1.94	±0.06
A7	Chondrule	BO	-2.9 $(n=5)$	±0.4	0.087	1.63	±0.02

* Bulk and matrix Mg isotope data represent <48 μm and <20 μm size fractions, respectively. These data were published earlier by Galy et al., (2000).

[†] POP = porphyritic olivine pyroxene; Al rich = aluminium rich mineralogy; PO = porphyritic olivine; BO = barred olivine.

[††] $\Delta^{17}O = \delta^{17}O - 0.52 \times \delta^{18}O$ where 0.52 is the ~ slope of the terrestrial fractionation curve. Uncertainty is the standard deviation for the average of n laser spot analyses per chondrule. Data collected according to methods described by Young et al., (1998a).

[‡] $^{27}Al/^{24}Mg$ was measured by MC–ICPMS with a precision of 2% relative.

[‡‡] Mg-isotopic compositions are expressed as per mil deviations from the international standard SRM 980. Uncertainties represent external analytical reproducibility. These data were published previously by Galy et al., (2000).

ICPMS data are unique in that they show *unequivocal* $\delta^{26}Mg*$ in the low Al/Mg minerals fassaite + spinel.

On the ^{26}Al–$^{26}Mg*$ evolution diagram (Fig. 13) analyses of unaltered material define a line with a slope corresponding to an initial $^{26}Al/^{27}Al$ of 6.3×10^{-5} (+/−1.8×10^{-5} 1σ) and an intercept of $\delta^{26}Mg* = 0.0$ +/−0.5. This evolution line and the corresponding initial $^{26}Al/^{27}Al$, or $(^{26}Al/^{27}Al)_0$, of 6.3×10^{-5} defined by the unaltered minerals is identical to the line obtained from the origin and a single acid-digestion MC–ICPMS measurement of a bulk CAI from Allende (Fig. 13, Galy et al., 2000). The canonical evolution line for carbonaceous chondrite CAIs has a slope corresponding to $(^{26}Al/^{27}Al)_0 = 5 \times 10^{-5}$ with a zero intercept (MacPherson et al., 1995). The evolution line defined by the laser ablation data is statistically distinct from the canonical line despite the large uncertainty in its slope that results from the limited range in Al/Mg spanned by the data. For example, if the slopes of the two lines are in fact the same, as permitted by the uncertainties, then the laser data define an initial $\delta^{26}Mg*$ of nearly 0.5‰ rather than 0.0 (Fig. 13).

The $(^{26}Al/^{27}Al)_0$ defined by both the laser ablation data and the bulk CAI datum is high but still within the range reported for CAIs (MacPherson et al., 1995). More data will be required to determine whether or not the high value for $(^{26}Al/^{27}Al)_0$ is an artefact of both the acid digestion and laser ablation MC–ICPMS measurements. A 20% systematic overestimation of the ratio of measured to actual $^{27}Al/^{24}Mg$ would be sufficient to bring the laser ablation data into alignment with the canonical $(^{26}Al/^{27}Al)_0$ value while maintaining a zero intercept. This level of Al/Mg fractionation has been observed under some experimental conditions (i.e., He carrier gas flow rates higher than those used in the present study).

The distinct $\delta^{25}Mg$ for analysis spot No. 1 suggests that alteration occurred in an open-system because closed-system Mg exchange would require a reservoir within the CAI that has lower $\delta^{25}Mg$ and lower $\delta^{26}Mg*$ than spot No. 1 and there is no such reservoir (a consequence of the low Al/Mg of this spot). In an open system deviations from the evolution line are expected because Mg is known to be more labile than Al, resulting in an increase in $^{27}Al/^{24}Mg$ at fixed $\delta^{26}Mg*$ in the altered zones. Leaching of Mg would likely be more efficacious

for the light isotope (a general result of transition state theory for reaction kinetics because greater vibrational frequencies lead to greater rate constants), resulting in mass-dependent fractionation to higher $\delta^{25}Mg$ and $\delta^{26}Mg$ at fixed $\delta^{26}Mg*$ (dashed line in Fig. 10) as the isotopically lighter Mg is carried away. The pre-leaching $^{27}Al/^{24}Mg$ of ≈1.6 (obtained by extrapolation to the primary evolution line at constant $\delta^{26}Mg*$ in Fig. 13) is within the range of values measured in the most Mg-rich fassaites from this CAI. The fact that the primary evolution line passes through the only high-precision bulk composition available for an Allende CAI (Fig. 13) suggests that magnesium loss from the CAI as a whole must have been negligible.

The new laser ablation Mg isotope data indicating that alteration occurred in an open system are consistent with the oxygen isotope data collected from this CAI that also appear to require open-system exchange during alteration. Laser ablation oxygen isotope ratio analyses of the altered areas in USNM 3576-1 show mass-dependent fractionations toward higher $\delta^{18}O$ analogous to the shifts in Mg isotopes reported here (Young and Russell, 1998). Increases in $\delta^{18}O$ associated with alteration were explained by Young et al. (1999) as being the result of open-system exchange with flowing aqueous fluid in the Allende parent body.

7. CONCLUSIONS

These experiments demonstrate the viability of using laser ablation in combination with MC–ICPMS as a tool for measuring Mg isotope ratios *in situ* in meteoritical materials. The advantages are high analytical precision combined with *in situ* sampling on the microgram scale, and independent measurements of both $\delta^{25}Mg$ and $\delta^{26}Mg$ at the 0.2‰ (2σ) level of precision.

First results show that mass-dependent variations in $^{25}Mg/^{24}Mg$ and $^{26}Mg/^{24}Mg$ in chondrules from the Allende meteorite are comparable to the mass-dependent variations seen in oxygen isotope ratios. Mixing of pre-chondrule materials with distinct Mg and O isotopic compositions and post-formation alteration both contributed to the variability in Mg isotope ratios in these objects.

The laser-ablation/MC–ICPMS method adds a new dimension to the analysis of Mg isotopes in CAIs. Dispersion around ^{26}Al–$^{26}Mg^*$ evolution lines can be correlated with petrography and Mg isotope mass fractionation in low-Al minerals, permitting distinction between open and closed-system behavior. This capability helps discriminate between those features of Al–Mg isotope systems that are relevant to chronology and those that result from element mobility.

Associate editor: U. Ott

REFERENCES

Ash R. D. and Young E. D. (2000) Clarity and confusion: the history of Allende chondrules as evinced by oxygen isotopes. *LPSC XXXI* abstr. 1881 (CD-ROM).

Ash R. D., Galy A., Young E. D., and O'Nions R. K. (2000) Correlated oxygen and magnesium isotopes in Allende chondrules. *Met. Planet. Sci.* **35,** A21.

Ash R. D., Young E. D., C. M. O'D. Alexander, Rumble D. III, and MacPherson G.J. (1999) Oxygen isotope systematics in Allende chondrules. *LPSC XXX* abstr. 1836 (CD-ROM).

Catanzaro E. J., Murphy T. J., Garner E. L., and Shields W. R. (1966) Absolute isotopic abundance ratios and atomic weight of magnesium. *J. Res. NBS-A: Phys. Chem.* **70A,** 453–458.

Clayton R. N., Onuma N., Ikeda Y., Mayeda T. K., Hutcheon I. D., Olsen E. J., and Molini-Velsko C. (1983) Oxygen isotopic comositions of chondrules in Allende and ordinary chondrites. In *Chondrules and Their Origins* (ed. E.A. King), pp. 37–43, Lun. Planet. Inst., Houston.

Cohen B. A., Hewins R. H., and Yu Y. (2000) Evaporation in the young solar nebula as the origin of 'just-right' melting of chondrules. *Nature* **406,** 600–602.

Davis A. M., Hashimoto A., Clayton R. N., and Mayeda T. K. (1990) Isotope mass fractionation during evaporation of Mg_2SiO_4. *Nature* **347,** 655–658.

Daughtry A. C., Perry D., and Williams M. (1962) Magnesium isotopic distribution in dolomite. *Geochim. Cosmochim. Acta* **26,** 857–866.

Galy, A., Belshaw, N. S., Halicz, L., and O'Nions, R. K. (2001) High-precision measurement of magnesium isotopes by multiple-collector inductively coupled plasma mass spectrometry (MC-ICPMS). *Int. J. Mass Spectrom.* **208,** 89–98.

Galy A. and O'Nions R. K. (2000) Is there a CHUR for Mg? *J. Conf. Abstr. (Goldschmidt 2000)* **5(2),** 424.

Galy A., Young E. D., Ash R. D., and O'Nions R. K. (2000) The formation of chondrules at high gas pressures in the solar nebula. *Science* **290,** 1751–1753.

Gray C. M. and Compston W. (1974) Excess ^{26}Mg in the Allende meteorite. *Nature* **251,** 495–497.

Lee T. and Papanastassiou D. A. (1974) Mg isotopic anomalies in the Allende meteorite and correlation with O and Sr effects. *Geophys. Res. Lett.* **1,** 225–228.

MacPherson G. J., Davis A. M., and Zinner E. K. (1995) The distribution of aluminum-26 in the early Solar System-a reappraisal. *Meteoritics* **30,** 365–386.

Sahijpal S., Goswami J. N., Davis A. M., Grossman L., and Lewis R. S. (1998) A stellar origin for the short-lived nuclides in the early Solar System. *Nature* **391,** 559–560.

Shima M. (1964) The isotopic composition of magnesium in terrestrial samples. *Bull. Chem. Soc. Jpn.* **37,** 284–285.

Weinbruch S., Palme H., and Spettel B. (2000) Refractory forsterite in primitive meteorites: condensates from the solar nebula? *Met. Planet. Sci.* **35,** 161–171.

Wood J. A. and Morfill G. E. (1988) A review of solar nebula models. In *Meteorites and the Early Solar System* (eds. J.F. Kerridge and M.S. Matthews), pp. 329–347, University of Arizona, Tucson.

Young E. D. (2000) Assessing the implications of K isotope cosmochemistry for evaporation in the preplanetary solar nebula. *Earth Planet. Sci. Lett.* **183,** 321–333.

Young E. D., Ash R. D., England P., and Rumble D. III (1999) Fluid flow in chondritic parent bodies: deciphering the compositions of planetesimals. *Science* **286,** 1331–1335.

Young E. D. and Russell S. S. (1998) Oxygen reservoirs in the early solar nebula inferred from an Allende CAI. *Science* **282,** 452–455.

Young E. D., Coutts D. W., and Kapitan D. (1998a) UV laser ablation and irm-GCMS microanalysis of $^{18}O/^{16}O$ and $^{17}O/^{16}O$ with application to a calcium-aluminium-rich inclusion from the Allende meteorite. *Geochim. Cosmochim. Acta* **62,** 3161–3168.

Young E. D., Nagahara H., Mysen B. O., and Audet D. M. (1998b) Non-Rayleigh oxygen isotope fractionation by mineral evaporation: theory and experiments in the system SiO_2. *Geochim. Cosmochim. Acta* **62,** 3109–3116.